PAPER

Check for updates

A bio-based PVA/phytic acid nanocomposite film with exceptional hydrogen barrier properties *via* free volume control

Sicheng Yuan, [ID]†[ab] Jintao Wei,†[ab] Junhao Zhou,†[e] Sheng Zhang,[ab] Baiwen Wang,[ab] Yanji Zhu[c] and Huaiyuan Wang [ID] *[abd]

Exploiting extremely low hydrogen permeability films is imperative for mitigating hydrogen damage and failure generated by strong hydrogen diffusion in storage vessels and pipelines. In this contribution, we have designed a simple yet effective strategy to fabricate a high-performance poly(vinyl alcohol) (PVA)-based composite thin film *via* a scalable spraying method, with the modification agent phytic acid (PA) incorporated to enhance crosslinking density. Various intermolecular interactions between PVA and PA form rigid structures that suppress chain mobility. Consequently, the fractional free volume (FFV) of the composite, as measured by positron annihilation lifetime spectroscopy (PALS), is reduced to merely 0.6509%. This leads to an unprecedented low H_2 gas transmission rate (GTR) of 0.518 cm^3 m^{-2}·24 h^{-1}·0.1 MPa^{-1}. These mutual interactions and mechanisms have also been corroborated by various simulation approaches and comprehensive experimental characterizations. Furthermore, this low H_2 GTR value exhibits no significant change even after 4 MPa hydrogen environment impact for 16 days, demonstrating high-pressure stability. Combined with a realistic coating process in the pipeline and a high mechanical tensile strength of 78 MPa, this composite thin film possesses tremendous application potential in hydrogen industries.

1 Introduction

Hydrogen is currently regarded as an essential industrial feedstock applied in diverse fields including fuel cells, aerospace, and automobiles.[1,2] In particular, hydrogen pipeline transportation is regarded as a future optimum delivery option from an economic perspective owing to its long-distance transportation viability.[3]

Nevertheless, the high diffusivity of hydrogen, owing to its extremely small molecular size, increases the risks of hydrogen leakage and correspondingly induced damage to metals.[4] It is mandatory to effectively mitigate this safety issue by 'wearing' protective shielding materials on metal substrates. In the field of H_2 barrier composite films/membranes/coatings, numerous researchers have adopted high-gas-barrier polymers, such as ethylene vinyl alcohol (EVOH),[5] polyurethane (PU),[6] polyamide 6 (PA6),[7] and thermoplastic polyurethane (TPU),[8] to cooperate with high-aspect-ratio nanosheets to further strengthen H_2 barrier performance. Regrettably, the H_2 gas transmission rate (H_2 GTR), the core evaluation indicator, of these materials is not sufficiently low to evade the negative effects of hydrogen diffusion. Recently, Liu *et al.*[9] employed innovative molecular patch engineering to fabricate a highly oriented polyethyleneimine (PEI)-modified graphene oxide (GO) membrane to achieve H_2 barrier performance. Assisted by abundant interactions between GO nanosheets and PEI, the assembled and highly aligned GO nanosheet sample exhibited a low H_2 GTR value of 4.2 cm^3 cm^{-2} s^{-1} Pa^{-1}, which also equals 3.6288 cm^3 m^{-2}·24 h^{-1}·0.1 MPa^{-1} at 25 °C. However, relying only on thousands of layers of GO and meticulously regulating their alignment to block H_2 molecules are costly and tedious, hindering industrial scalability and future pipeline applications.

It is thought-provoking what kinds of materials can be selected and paired to realize high H_2 blocking efficiency by a

[a] School of Chemical Engineering and Technology, State Key Laboratory of Chemical Engineering, Tianjin University, Tianjin 300350, PR China. E-mail: huaiyuanwang@tju.edu.cn

[b] Tianjin Key Laboratory of Chemical Process Safety and Equipment Technology, Tianjin University, Tianjin 300072, PR China

[c] School of Materials Science and Engineering, Tianjin University, Tianjin 300072, PR China

[d] Ningbo Key Laboratory of Green Petrochemical Carbon Emission Reduction Technology and Equipment, Zhejiang Institute of Tianjin University, Ningbo, Zhejiang 315201, PR China

[e] MOE Key Laboratory of Cluster Science, Beijing Key Laboratory of Photoelectronic/Electrophotonic Conversion Materials, School of Chemistry and Chemical Engineering, Beijing Institute of Technology, Beijing 102488, PR China

† Sicheng Yuan, Jintao Wei, and Junhao Zhou contributed equally to this work.

facile and cost-effective method. Poly(vinyl alcohol) (PVA) is an extensively applied barrier polymer in the food packaging field because of its excellent O_2 barrier property.[10,11] This is attributed to its strong intermolecular interactions and semi-crystalline nature.[12] Furthermore, beyond its barrier capabilities, PVA has also been demonstrated to exhibit good corrosion resistance, forming protective coatings that can shield metal substrates from corrosive environments.[13] Most importantly, most previous studies have endeavoured to fortify its O_2 and CO_2 barrier performance in humid environments and strengthen its water resistance.[14] However, investigations into its H_2 barrier performance and corresponding improvement strategies are still in their infancy, which endows us with numerous opportunities to explore the possibility of its application in this field.

Moreover, it is theoretically plausible to further enhance its H_2 barrier performance by introducing crosslinkers in the PVA composite system by learning from other literature studies on gas-blocking performance optimization methods. Specifically, various acids such as boric acid,[15] citric acid,[16] and oxalic acid[17] were incorporated into a PVA-based composite system to improve its O_2 barrier performance and other properties. The creation of more compact and rigid chain structures, facilitated by crosslinking reactions, contributed to upgrading its O_2 barrier performance.[14,18] Phytic acid (PA) is a macromolecular additive that is completely bio-derived, nontoxic, and easily accessible from plant sources, and it has more hydroxyl groups than other synthetic acids and hence is anticipated to more actively engage in crosslinking reactions with PVA polymer chains *via* abundant noncovalent and covalent chemical interactions. Therefore, the resulting high crosslinking density of the modified system may have a positive influence on H_2 diffusion inhibition. The theoretical simulation and experiments conducted by Li *et al.* on the elaborate chain dynamics and interactions between PVA and PA provide vital inspiration on the viability of PA as a gas barrier performance enhancer from a mechanistic aspect.[19] This modification agent's influence on the H_2 barrier performance remains intriguing and is worthy of thorough clarification. Additionally, the interplay between the crystallinity and the FFV, two crucial parameters that govern the gas barrier property of composites, remains unambiguously unexplored and requires clarification.

In our approach, PA is employed as a crosslinking reagent to fabricate PVA–PA composite thin films by a facile spraying method. The effects of different PA contents in the composite system on its H_2 barrier performance and other properties are explicitly surveyed. Consequently, the optimum sample, PVA–20PA, exhibits an exceptionally low H_2 GTR value of 0.518 cm^3 m^{-2}·24 h^{-1}·0.1 MPa^{-1} and a minimal FFV of 0.6509%, as quantitatively measured by PALS. The abundant intermolecular interactions between PVA and PA, rigorously evidenced by various characterization methods and further supported by comprehensive simulations, promote the formation of a tightly crosslinked network, effectively reducing the free volume in the PVA chain. We have also elucidated

that the determining factor affecting the H_2 barrier performance of PVA is the FFV rather than crystallinity. In addition, the optimal sample maintains its remarkable H_2 barrier property with an H_2 GTR value of 0.966 cm^3 m^{-2}·24 h^{-1}·0.1 MPa^{-1} even after exposure to a harsh 4 MPa hydrogen environment for 16 days. The high mechanical tensile strength of 78 MPa also synergistically endows this PVA–PA composite film with tremendous practical application prospects.

2 Results and discussion

2.1 Chemical and structural characterizations

The detailed preparation process of the composite film is shown in Fig. 1a. The water-bath heating and ultrasonic treatment ensured the complete hydrolysis and reaction of the PVA–PA mixture. Moreover, the PVA–PA-coated graphite paper is expected to possess better mechanical stability, with no visible cracking phenomenon observed after hand-bending. In contrast, the uncoated graphite paper presents noticeable fractures (as shown in the insets of Fig. 1a). The plant-based origin of PA, the biodegradability of PVA, and the entirely water-based process collectively ensure environmental friendliness throughout the preparation cycle, paving the way for large-scale applications with a low carbon footprint.

The scalable spray-coating method, while advantageous for future applications, is susceptible to defect formation, such as pinholes, cracks, or inhomogeneities, if the parameters are not optimized. These defects can serve as fast pathways for gas permeation, severely compromising barrier performance.[20] In this work, several strategies were employed to mitigate such defects: (1) solution preparation: ultrasonic treatment was applied to the PVA–PA mixture to ensure a homogeneous and well-dispersed solution, preventing the aggregation of components that could act as defects. (2) Optimized spray parameters: the combination of a low-solid-content solution, an appropriate spray distance, and a heated substrate (140 °C) was crucial. This setup promoted rapid solvent evaporation upon droplet impact, "freezing" the film structure instantly and minimizing the time for phase separation or uneven flow, which leads to defects like 'orange-peel' morphology. (3) Multiple thin passes: instead of a single thick coating, we applied multiple light passes. This approach allowed each layer to dry and form a continuous network before the next was applied, effectively "healing" potential minor imperfections in the underlying layer and resulting in a denser, more integral final film. (4) *In situ* crosslinking: the elevated substrate temperature not only aided drying but also promoted the crosslinking reaction between PVA and PA during film formation. This created a robust network that enhanced mechanical integrity and reduced the likelihood of crack formation during handling or under stress.

Therefore, the resultant high quality of the films, as evidenced by the dense and uniform SEM morphologies (Fig. S4a4 and a5), the visible smooth surface in the digital picture captured by a smartphone (Fig. S3), and the homogeneous
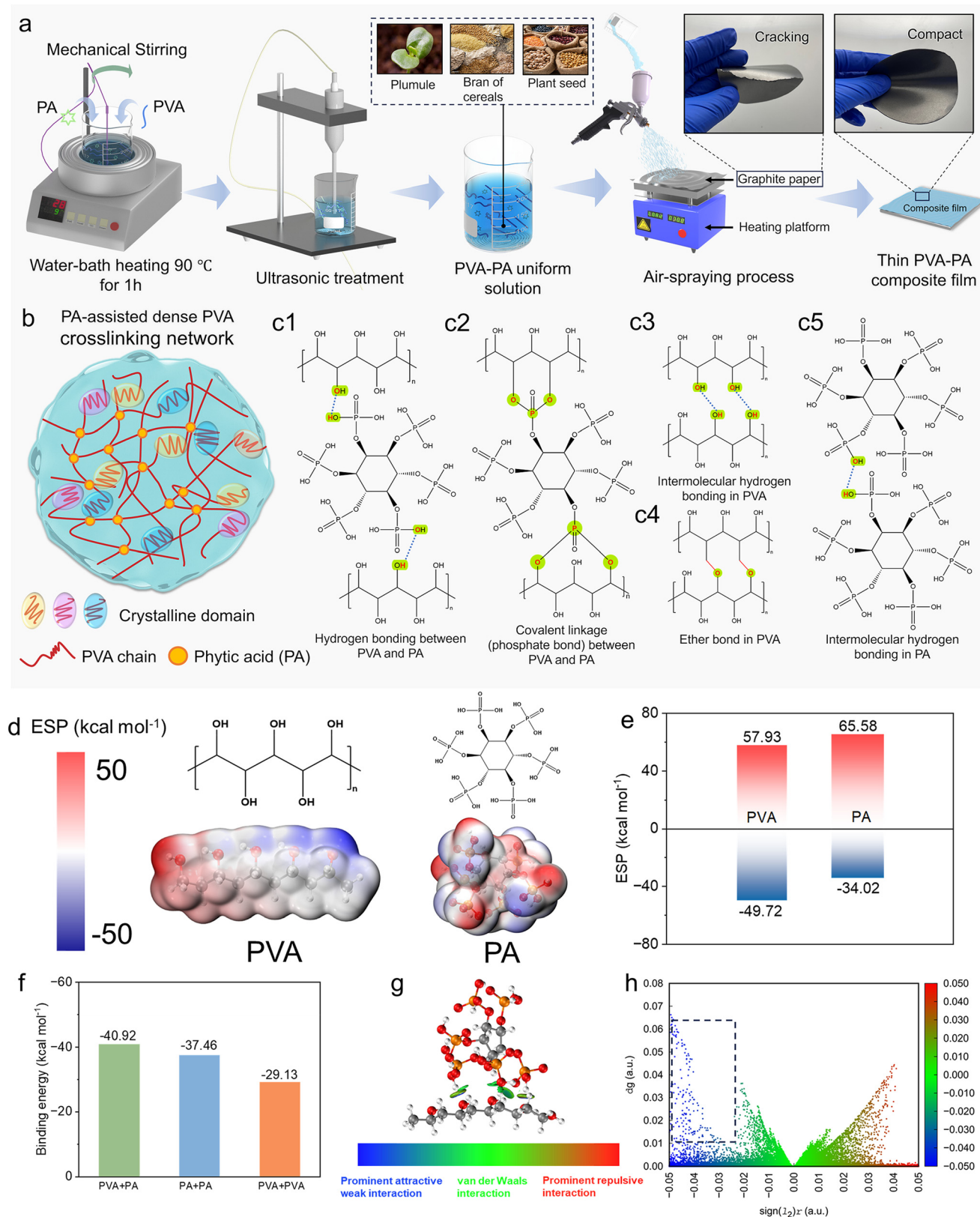
Fig. 1 (a) The preparation procedure of the PVA–PA composite thin film; insets show the illustration that PA mainly originates from plumules, bran of cereals, and plant seeds and the comparison between coated and uncoated graphite paper; (b) the graphical representation of the formed crosslinking network between PVA and PA; (c1) hydrogen bonding between PVA and PA; (c2) phosphate bond between PVA and PA; (c3 and c4) intermolecular hydrogen bonding and ether bond in PVA, respectively; (c5) intermolecular hydrogen bond in PA; (d) electrostatic potentials (ESPs) and molecular structures of PVA and PA; (e) the maximum and minimum ESP distributions of PVA and PA; (f) the DFT calculations for the binding energies of PVA to PA, PA to PA, and PVA to PVA; (g) the IGMH analysis of PVA and PA; and (h) the IGMH scatter plot of PVA and PA.

elemental distribution (Fig. S4a1–a3), coupled with the exceptionally low and reproducible H$_2$ GTR values, strongly indicates that defects have been effectively minimized in our optimized process.

2.1.1 FT-IR analysis. As displayed in Fig. 2a, the pure PVA film exhibits significant and characteristic peaks at 3290 cm^{-1} and 2940 cm^{-1}, which are associated with the –OH and C–H groups in the PVA chain, respectively.[11,21] Additionally, the peak at around 1087 cm^{-1} represents the C–O bond stretching vibration of the residual nonhydrolyzed vinyl acetate group on PVA.[22,23] Noticeably, the absorption band at 1143 cm^{-1} is attributed to the typical crystallisation peak frequently employed to evaluate the crystallinity changes in the PVA structure.[24] Another characteristic peak found at 915 cm^{-1} is attributed to the syndiotactic structure and skeleton of PVA.[25] After the introduction of PA, the peak located at 3290 cm^{-1} shifts to a lower wavenumber for all PA-incorporated samples, suggesting strong intermolecular hydrogen bonding interactions between the hydroxyl groups on PVA and PA (Fig. 1c1).[26] A newly emerged peak at 996 cm^{-1} can be observed for the PVA/PA composite film when the added PA amount exceeds 0.2 g. This band is direct evidence of the existence of the P–O–C bond and the covalent linkage between PA and PVA by a phosphonate structure (Fig. 1c2), indicating the successful formation of a crosslinking network.[27] However, the esterification reaction between the hydroxyl groups on the PVA chain and the phosphonic acid groups of PA is less likely to happen with insufficient incorporation of PA (0.2 g), leading to the absence of the absorption band at 996 cm^{-1}. It should also be noted that the bands at 1087 cm^{-1} and 1709 cm^{-1} (the evidence of the C=O bond[28,29]) vanish for all the composite films with gradually increasing PA ratio. This may be due to the generation of ether bonds *via* hydrolysis between various PVA chains in acid environments (Fig. 1c4).[10,30] It is boldly extrapolated that the nonhydrolyzed vinyl acetate group of PVA experiences gradual hydrolysis, and the formation of ether bonds demonstrates the intermolecular interactions between PVA chains.
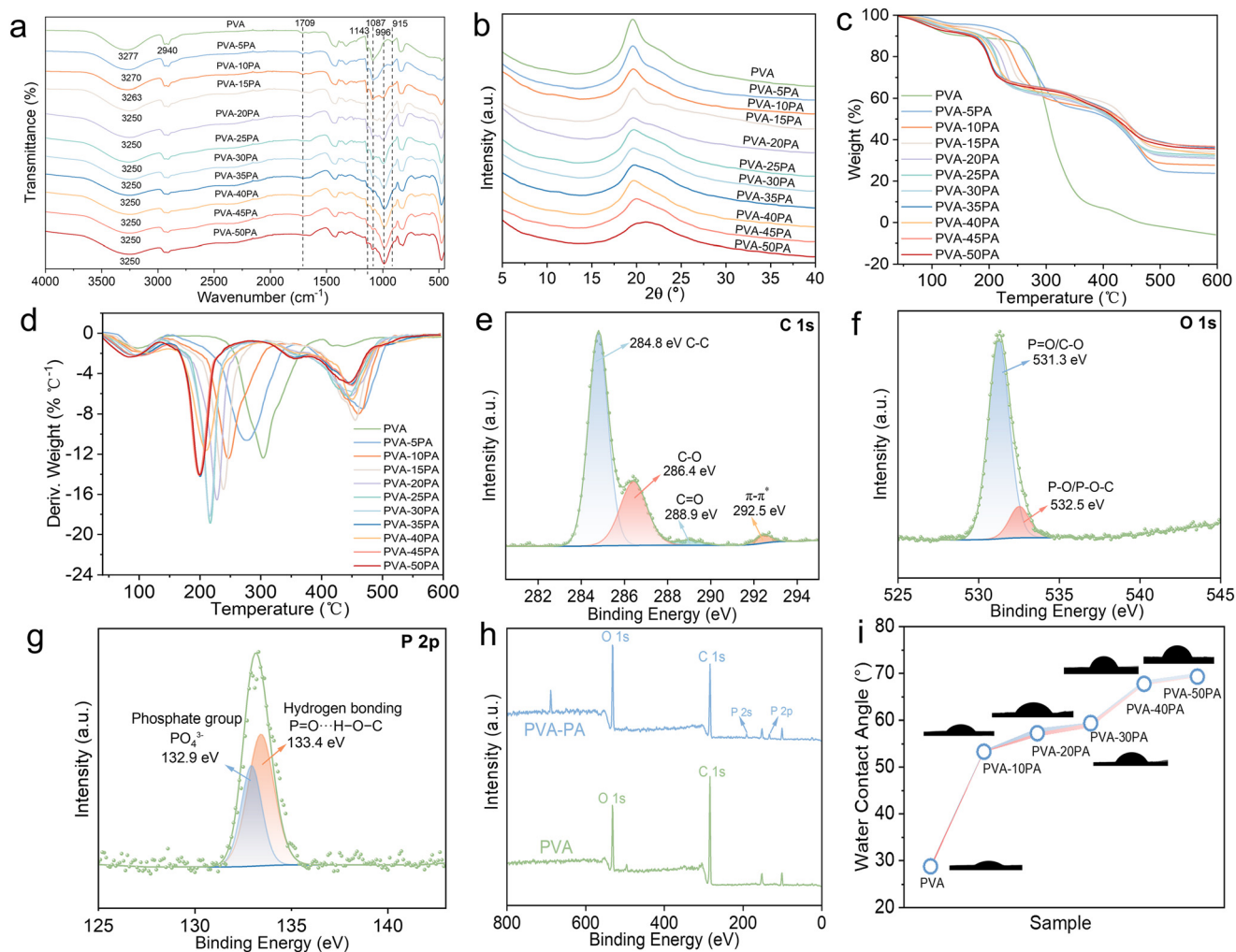

Fig. 2 Structural and surface characterization of the PVA–PA composite films: (a–d) FTIR spectra, XRD patterns, TGA curves, and DTG curves of PVA–PA with different PA contents, respectively; (e–g) C 1s, O 1s, and P 2p XPS spectra of PVA–20PA; (h) overall XPS spectra of PVA–20PA and PVA; and (i) water contact angles (WCAs) of PVA and the PVA–PA samples with various PA percentages.

Most importantly, the phenomenon that the intensity of the crystallisation-sensitive peak at 1143 cm^{-1} shows a weakening trend with increasing PA addition suggests that the introduction of foreign molecules has a negative impact on the intermolecular hydrogen bonding between PVA chains (Fig. 1c3). The formation of these new interactions can impair the crystalline structure of pure PVA and weaken its crystallinity.[31,32]

To further determine the mutual noncovalent interactions between PVA and PA, DFT was implemented to compare the electrostatic potential (ESP) distributions of PVA and PA, as exhibited in Fig. 1d. The calculated results reveal that PA possesses the most positive ESP value of 65.58 kcal mol^{-1}. In comparison, PVA demonstrates the most negative ESP value of -49.72 kcal mol^{-1} (Fig. 1e), evidencing the strong affinity between them. Therefore, the PVA–PA combination exhibits the highest binding energy with a value of -40.92 kcal mol^{-1} (Fig. 1f), also suggesting that PVA preferentially interacts with the PA molecule. In addition, hydrogen bonding is identified as the dominant force between PVA and PA, as evidenced by peaks in the sign$(\lambda_2)\rho < 0$ region (dashed rectangle) of IGMH 2D scatter plots (Fig. 1g and h).

To conclude on the structural changes after the introduction of PA, the PVA chain and the PA can interact *via* phosphonate bonds, while intermolecular hydrogen bonding can also be generated between hydroxyl groups. Moreover, the ether bond between various PVA chains in the presence of PA has been verified. The intermolecular H-bonding interactions in PA molecules (Fig. 1c5) can also be generated to synergistically promote the development of a dense crosslinking network and mutual interactions (Fig. 1b).

2.1.2 XRD analysis. In Fig. 2b, the intense peak at around $2\theta = 19.5°$ belongs to the (101) characteristic diffraction peak of PVA, ascribed to the abundant and strong intermolecular hydrogen bonding between hydroxyl groups in the repeating units of PVA chains.[30] However, the intensity of the peak at 19.5° reveals a decreasing trend as the weight ratio of PA increases, with the sharp peak gradually transforming into a shoulder peak. This is because the introduction of foreign molecules is capable of inhibiting and disrupting the original intermolecular hydrogen bonding between PVA chains and constructing new mutual interactions. Consequently, this crosslinking effect between PVA and PA through phosphonate bonds as well as hydrogen bonding and intermolecular ether bonds between PVA chains collaboratively prevent crystalline region establishment and therefore reduce the degree of crystallinity, which is consistent with the FT-IR analysis of the crystalline-sensitive peak of PVA at 1143 cm^{-1}.

2.1.3 TGA analysis. To investigate the thermal stability of the PVA film and PA-incorporated composite films with different contents, thermogravimetric (TGA) and derivative thermogravimetric (DTG) tests were carried out under a N$_2$ atmosphere. As displayed in Fig. 2c, before the temperature reaches 100 °C, the adsorbed water molecules are mainly eliminated. In the temperature range from 100 °C to 230 °C, the weight loss is not evident, and the molecular structure of PVA is not destroyed. Afterwards, the weight of PVA suffers

from a sharp decrease from 250 °C to 370 °C, and the TGA curve exhibits the largest slope, which represents the depolymerization process of the PVA molecular chain. The temperature of the first maximum degradation rate ($T_{max,1}$) is around 305.83 °C (obtained from Fig. 2d). When the temperature exceeds 370 °C, the C–C skeleton of PVA is fully destroyed and converted to CO and CO$_2$ during the cyclization process.[33] Noticeably, all PA-incorporated samples exhibit lower $T_{max,1}$ values than pure PVA and an overall gradually decreasing trend with increasing PA content (detailed information can be found in Table S1), which is highly associated with the PA-assisted catalytic decomposition in the early stage of PVA degradation owing to the existence of phosphorus groups in PA.[34] The crystallinity reduction of PVA induced by PA introduction also promotes loose structure formation, leading to faster free-bound water evaporation.[24] In addition, the temperature at which 5% weight loss of PVA takes place ($T_{5\%}$) is approximately 93.83 °C. The introduction of PA significantly increases the $T_{5\%}$ at all contents except for the highest PA content (50 wt%), which is attributed to the carbon layer's enhanced thermal stability caused by PA catalytic degradation.[34] Also, the char residue of all PA-incorporated composite films is greatly increased compared to that of pure PVA, with PVA–45PA possessing the highest percentage of char residue. In the meantime, the maximum weight loss rate of all PVA–PA composite films reveals a decreasing tendency compared with pure PVA. Furthermore, the slopes of the weight loss curves of all PVA–PA composite films are conspicuously lower than that of pure PVA, demonstrating that PVA–PA composites possess better thermal stability.

The aforementioned data and analysis provide strong evidence for the improved thermal stability of PVA–PA samples. Primarily, the strong intermolecular covalent linkage, P–O–C bond, and noncovalent hydrogen bonding between PVA and PA, as evidenced by FTIR and XPS, can effectively prevent or hinder the thermal degradation of PVA.[30] In addition, the ether bonds formed by the dehydration of various PVA chains play positive roles in improving thermal stability.[10] Further, the higher level of char residue for all PA-incorporated composite samples, compared with pure PVA, results from more effective dehydration carbonization and OH radical capture induced by the phosphate substance from PA.[35]

2.1.4 XPS analysis. The XPS spectra of pure PVA and PVA–PA were further analysed to investigate the chemical structures and mutual interactions between PVA and PA. As shown in Fig. S2, the pure PVA film displays three curve-fitted characteristic peaks at 284.8 eV, 286.4 eV, and 288.9 eV in the C 1s spectrum, which are ascribed to the C–C, C–O, and C=O bonds, respectively.[36] The presence of the C=O bond indicates the incomplete hydrolysis of ethyl acetate during the PVA manufacturing process. In addition, it presents only a single peak at 531.5 eV, associated with the C–O and C–O–C bonds in the O 1s spectrum.[37] By comparison, there are four deconvoluted peaks for the PVA–PA sample in the C 1s spectrum (Fig. 2e), from which the satellite peak at 292.5 eV stands out. It is attributed to the intermolecular noncovalent

π–π^* bonding due to the existence of a benzenoid ring in the PA molecule,[38] which evidences that the incorporation of PA not only generates intermolecular interactions with PVA (covalent and hydrogen bonding) but also induces its own intermolecular noncovalent bonding. The small peak with a binding energy of 532.5 eV in the O 1s spectrum corresponds to the P–O–C/P–O bonding (Fig. 2f),[39] consistent with the FTIR analysis of covalent interactions. The partially deprotonated state of the phosphate groups, as inferred from the O 1s XPS peaks, suggests the potential for ionic or electrostatic interactions with the hydroxyl groups of PVA.[40] This ionic component can further strengthen the crosslinking network, adding another layer of restriction on chain dynamics. The intermolecular hydrogen bonding between PVA and PA can also be verified by the peak at 133.4 eV (ref. 41) in the P 2p spectrum, while another peak located at 132.9 eV represents the phosphate group from the PA (Fig. 2g) molecule.[42] Comparing the overall spectra of PVA and PVA–PA, two small peaks belonging to the P 2p and P 2s orbitals are evident (Fig. 2h).

2.1.5 Surface analysis. The water contact angle (WCA) of PVA and some PVA–PA samples was measured and is exhibited in Fig. 2i. It increases moderately from around 28.75° for pure PVA to 69.25° for PVA–50PA (detailed measurement results are provided in Fig. S7). This consistent rise is a direct indicator of the successful crosslinking reaction between PVA and PA. The reaction consumes the hydrophilic hydroxyl (–OH) groups of PVA, converting them into covalent P–O–C bonds and integrating them into the network structure with the more complex, cyclic PA molecule. This process reduces the overall surface energy and the density of polar groups available to interact with water, thereby rendering the composite film's surface less hydrophilic. However, the flat surface morphology and uniform C, O, and P elemental distribution, captured by scanning electron microscopy (SEM) and corresponding energy-dispersive X-ray (EDX) spectra, indicate the successful fabrication of this hybrid film (Fig. S4a1–a6). The corresponding scanned elemental weights and atomic percentages are revealed in the inset of Fig. S4a6. The thickness of this hybrid film is roughly 6.2 μm, as seen from the cross-sectional SEM image in Fig. S4a5.

2.2 Hydrogen gas barrier property and overall comparison

The H$_2$ gas transmission rate (GTR) was employed to assess the H$_2$ barrier property of PVA and composite films, according to GB/T 19789-2021. The graphite paper was selected as a substrate for sprayed composite films because it was fully permeable without barrier properties against H$_2$ molecules. Therefore, the acquired test data directly reflected the actual H$_2$ barrier performance of the fabricated films. As shown in Fig. 3a, pure PVA exhibits a H$_2$ GTR value of 2.11 cm^3 m^{-2}·24 h^{-1}·0.1 MPa^{-1}. PVA's low H$_2$ permeation value is attributed to its high degree of crystallinity and strong intermolecular hydrogen bonding forces. Later, this value shows a gradually decreasing trend to the lowest value of 0.518 cm^3 m^{-2}·24 h^{-1}·0.1 MPa^{-1} for the PVA–20PA sample, representing a

~75.5% reduction compared to the pure sample. By contrast, it constantly increases to 2.275 cm^3 m^{-2}·24 h^{-1}·0.1 MPa^{-1} at the highest PA content. Similarly, the PVA–20PA sample exhibits the lowest H$_2$ permeability coefficient of 6 × 10^{-12} cm^3 cm m^{-2} s^{-1} Pa^{-1} (Fig. 3b). The permeation curves, captured by the permeation testing machine, presented in Fig. 3c also provide solid evidence of these extraordinarily low H$_2$ permeation values. The ending lower-chamber pressure of PVA–20PA is lower than 15 Pa after an 8 hour consecutive H$_2$ permeation process, while that of pure PVA exceeds 40 Pa in the same period.

The deterioration of the H$_2$ barrier property beyond the optimal PVA–20PA composition, despite a continued increase in the crosslinker content, can be attributed to microstructural changes induced by excessive PA. We propose a multifaceted mechanism: firstly, the surplus of unreacted PA molecules at a high loading (e.g., 50 wt%) can act as plasticizers, enhancing the polymer chain mobility and dynamic free volume, thereby facilitating gas diffusion.[43] Secondly, an exceedingly high crosslinking density can lead to a heterogeneous network. The formation of locally over-crosslinked clusters may introduce nanoscale stress and defects, such as microvoids at the interfaces between domains of different crosslinking densities.[44] These defects can serve as efficient pathways for gas permeation. Consequently, the positive effect of a denser network is counteracted and surpassed by these negative consequences of over-crosslinking, leading to a net increase in the FFV and H$_2$ permeability for PVA–50PA.

Comparing the absolute H$_2$ GTR value with previously reported studies on polymer-based H$_2$ barrier membranes/coatings/films and other commercial gas barrier products is beneficial for understanding the level that our work has achieved and highlighting our work's advantage. As shown in Fig. 3d, many works employed chemically modified graphene oxide (GO) and MXenes as two-dimensional nanofillers to incorporate into various polymer matrices to construct H$_2$ barrier composite systems. However, the H$_2$ GTR values in most research studies are distributed in high and medium levels, suggesting that the barrier enhancement ability of sheet-like fillers is limited. The H$_2$ GTR value of our optimal film represents a top-tier level of barrier performance, as it is lower than that of most reported polymer-based composites and comparable to that of the best-performing systems (see Table S3 for a detailed comparison).

Positron annihilation lifetime spectroscopy (PALS) was employed to determine the FFV in the composite system, which is mainly responsible for gas diffusion and transport. The ortho-positronium (o-Ps) pickoff lifetime (τ_3) and its intensity (I_3) can be related to the size (pore radius r) and density of nanoholes in the composites. As can be seen in Fig. 3f, the τ_3 and free volume hole radius r present similar rising tendencies, with PVA–50PA exhibiting the largest values of τ_3 (1.553 ns) and r (0.239 nm). Contrastingly, the I_3 gradually declines with more PA incorporation, while the FFV value first decreases from 0.7176% to 0.6509% and then increases to 0.7161%. It has been clarified that the distribution of free
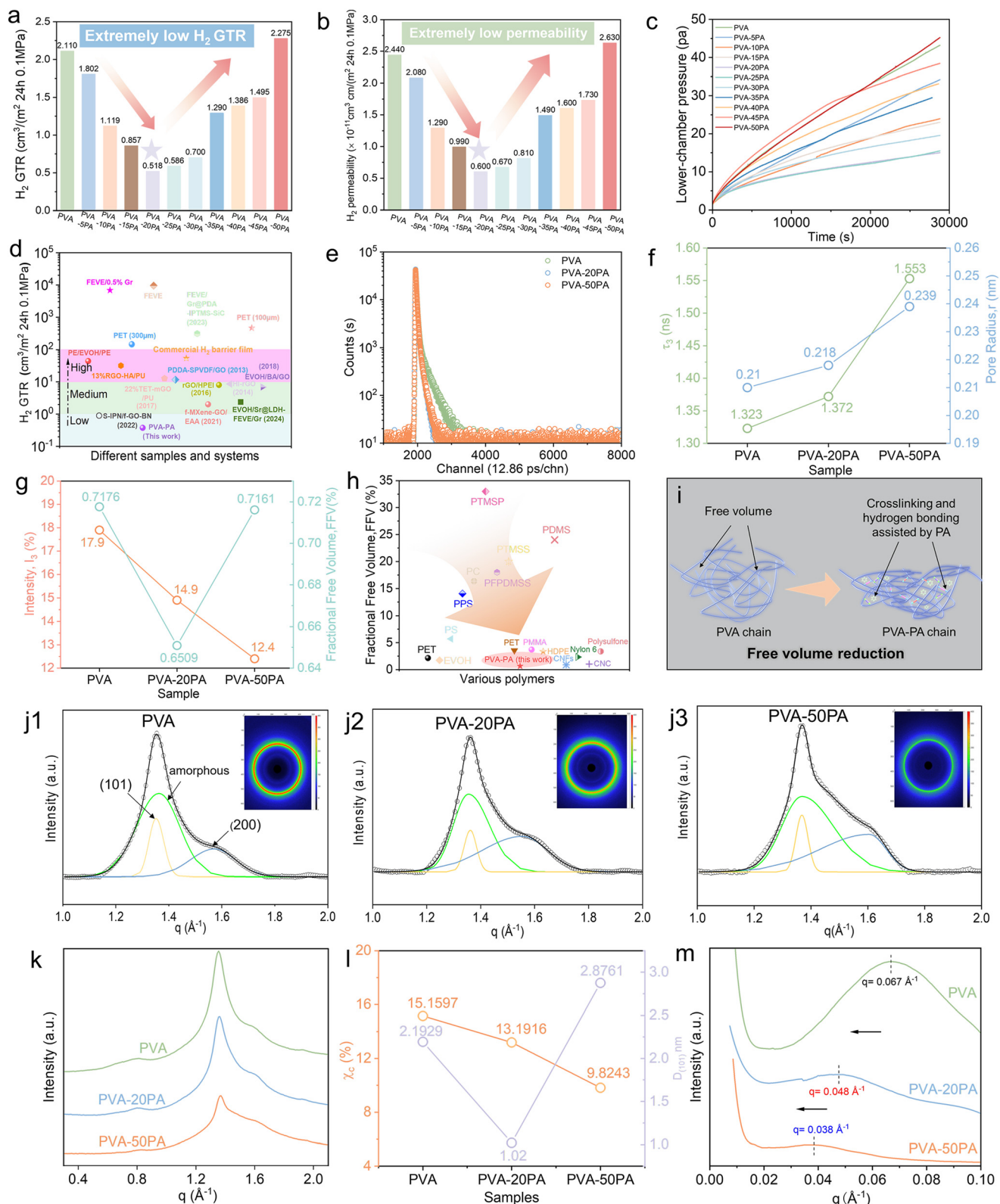
Fig. 3 (a and b) H$_2$ GTR and permeability values of PVA and diverse PVA–PA samples; (c) the instrument-generated permeation curves (lower chamber pressure as the function of time) of all the specimens; (d) the comprehensive comparison of the H$_2$ GTR values from this work with other researcher works; (e) the measured positron lifetime spectrum and the three-component τ_3 fitting curve for PVA, PVA–20PA, and PVA–50PA; (f) τ_3 and pore radius r of PVA, PVA–20PA, and PVA–50PA; (g) I_3 intensity and FFV of PVA, PVA–20PA, and PVA–50PA; (h) comparison of the FFV value of PVA–20PA with other materials; (i) free volume reduction effect of PVA assisted by PA crosslinking and hydrogen bonding interactions; and (j1–j3) multipeak fitting analysis of the WAXS curves, deconvoluting the (101) and (200) crystal planes. The corresponding 2D scattering patterns are the inset in each panel. (k) The corresponding 1D integrated WAXS curves; (l) the calculated crystallinity χ_c and lateral crystal size of the (101) crystal plane $D_{(101)}$; and (m) SAXS patterns of PVA, PVA–20PA, and PVA–50PA.

volume holes and their size collaboratively exert an impact on the FFV.[45] The trend for the FFV complies with the H_2 GTR variation tendency, with PVA–20PA exhibiting the lowest H_2 GTR and FFV values. Even a slight change in the FFV value tends to have a significant influence on the gas transport property.[46] Besides, this FFV value reaches an extremely low level compared to common engineering and barrier polymers (EVOH, HDPE, *etc.*), representing the superiority of this work (Fig. 3h). Other detailed information from PALS is provided in Table S2.

The wide-angle X-ray scattering (WAXS) test of the same samples was conducted to clarify the crystal structures of PVA and composite films both quantitatively and qualitatively. Multiple-peak fitting analyses were utilized on the 1D integrated WAXS curves for quantitative analysis, as displayed in Fig. 3j1–j3. The typical diffraction peaks for the (101) and (200) crystal planes were accordingly deconvoluted. The existence of the (101) crystal plane contributes to the gas barrier property of the PVA film.[47] Therefore, the crystallinity χ_c, determined using the ratio of the area of the (101) crystal plane in the deconvolution results and its lateral crystal size (D_{101}), is summarized in Fig. 3l. The WAXS peak intensity of PVA, PVA–20PA, and PVA–50PA (Fig. 3k) exhibits a gradually weakening trend analogous to the decreasing tendency of χ_c from 15.1597% to 9.8243%. Meanwhile, the 2D WAXS scattering ring shows the corresponding attenuation with increasing percentage of PA as the red colour becomes lighter. Even though the crystal size of the (101) crystal plane, calculated by the Scherrer equation (detailed calculation process can be found in the SI), first reduces to 1.02 nm and then increases to 2.8761 nm, it can still be firmly concluded that the crystalline structure destruction effect due to the PA-assisted crosslinking reaction with PVA occurs.

The small-angle X-ray scattering (SAXS) result of PVA indicates a single peak at a scattering vector of 0.067 Å^{-1}, attributed to its semicrystalline structure. The gradual absence and blur of the observed peak for PVA–20PA and PVA–50PA (Fig. 3m) demonstrate a significant reduction in the polymer crystallinity as well.[48] As the PA content increases, the electron density contrast between crystalline and amorphous phases and the lamellar correlation both decrease, indicating the progressive weakening of the lamellar semicrystalline structure; at 50 wt% PA, it is the weakest, tending toward a more amorphous network. The long period L can be determined by the electron density correlation function $\gamma(r)$ curves using the Fourier transformation. In the meantime, the lamella thickness d_c is obtained by L times the crystallinity χ_c. Then, the subtraction of the crystalline thickness d_c from the long period L yields the interlamellar spacing d_a. The corresponding plots and calculated results are presented in Fig. S8–S10. The synergistic reduction tendency of L, d_c, and d_a implies the gradual destruction of PVA crystals, which is also consistent with the progressive attenuation of the SAXS diffraction ring (Fig. S12–S14). Overall, SAXS results also confirm the attenuation of lamellar semicrystalline structures with increasing PA content.

In conclusion, the apparent paradox—where a significant decrease in the composite film's crystallinity (as evidenced by XRD and WAXS/SAXS) coincides with a significant improvement in hydrogen barrier performance (Fig. 3a)—is unequivocally resolved by pinpointing the fractional free volume (FFV) with an ultralow value of 0.6509% as the decisive factor consequently, the outstanding hydrogen barrier performance is unequivocally governed by this FFV reduction, establishing it as the dominant mechanism that supersedes the traditional role of crystallinity.

2.3 High-pressure hydrogen tolerance and comprehensive performance

Most gas impermeability tests are performed at ambient pressure and lack higher-pressure evaluation. However, whether the prepared composite film can withstand the impact of a pressurized hydrogen environment is worthy of scrutiny to meet the requirements of practical hydrogen transportation. The operation pressure varies from 3 to 5 MPa, and the pipeline is made of multiple steels including ASTM 106, API 5L Grade B, and modern X42/X52 steel.[49] China is also advancing the development of pure hydrogen pipelines with abundant projects, in which the Wuhai-Yinchuan project stands out because of its longest distance of around 217.5 km.[3,50] The operating pressure is below 4 MPa because safety issues have been the primary concern. Therefore, several samples were sealed in an autoclave with a hydrogen pressure of approximately 4 MPa for 16 days. Later, the tested specimens were again appraised by hydrogen permeation tests to determine the influence of 4 MPa hydrogen conditions on various composite films.

As displayed in Fig. 4b, the H_2 GTR of pure PVA increases sharply from 2.11 cm^3 m^{-2}·24 h^{-1}·0.1 MPa^{-1} to 13.272 cm^3 m^{-2}·24 h^{-1}·0.1 MPa^{-1} after this high-pressure hydrogen shock experiment. Although other PA-incorporated composite films also reveal a similar increasing trend, compared with the original samples, their growth rate is not as evident as that of pure PVA, in which PVA–20PA is noticeable because it still exhibits at an extremely low H_2 GTR level of 0.966 cm^3 m^{-2}·24 h^{-1}·0.1 MPa^{-1}. Its corresponding permeation curve also shows a sluggish lower-chamber pressure growth rate (Fig. 4a). Specifically, the free-volume holes of PVA will be largely occupied because of the drastic accumulation of H_2 molecules under the effect of high-pressure hydrogen aggression, whereas the PVA–PA compact crosslinking network promoted by multiple noncovalent and covalent interactions still displays extraordinary high-pressure hydrogen resistance, with fewer hydrogen molecules invading into the free-volume voids (Fig. 4i).

Regarding the surface morphology after high-pressure hydrogen exposure, macroscopically, the supported films exhibit a fine wrinkling pattern (Fig. S15a), a common viscoelastic response to the compressive stresses during the pressurization-depressurization cycle. Crucially, however, scanning electron microscopy (SEM) analysis confirms that the surface of the PVA–20PA film remains smooth and continuous at the
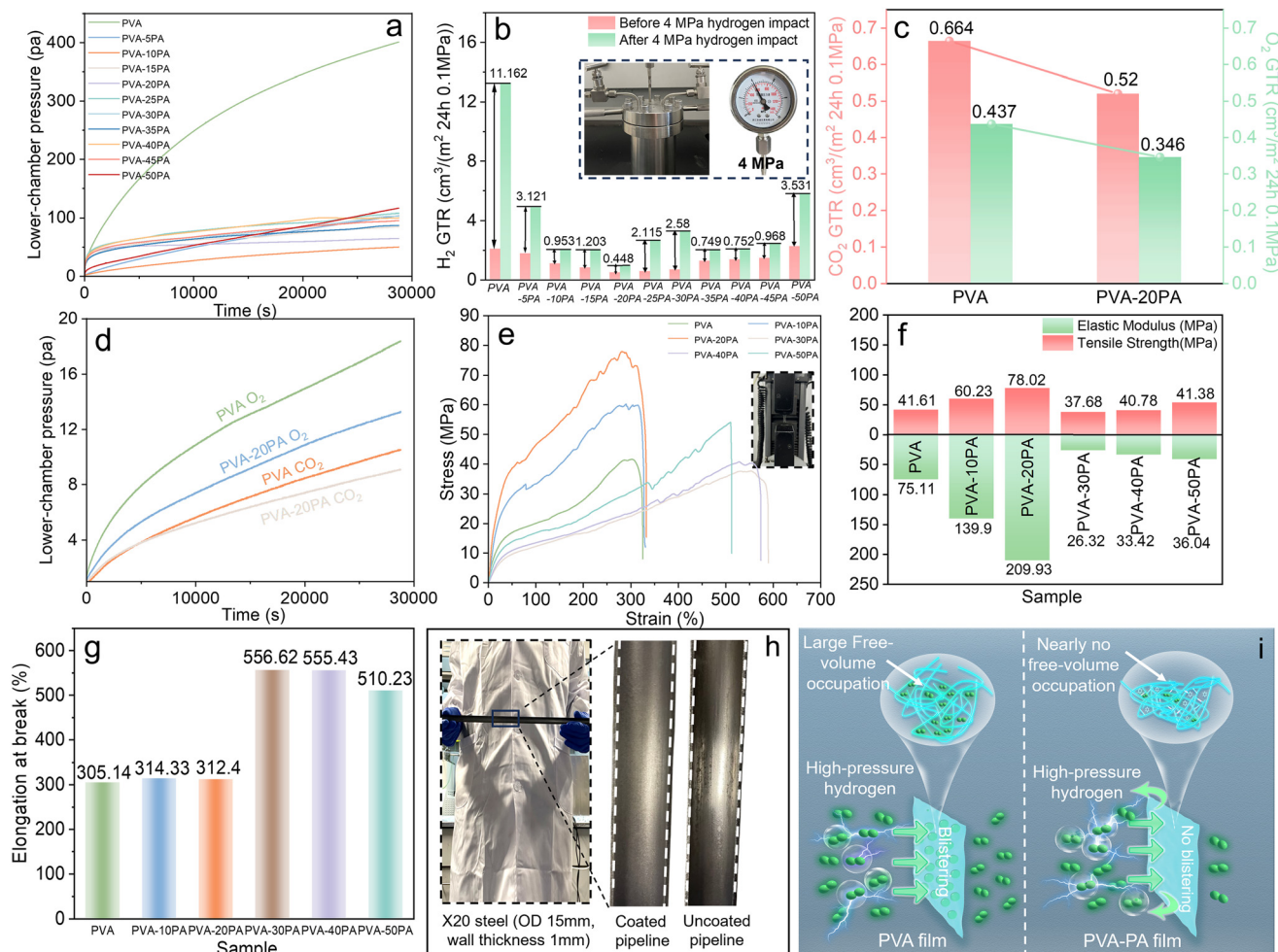
Fig. 4 (a and b) Instrument-generated permeation curves of all samples after 4 MPa hydrogen impact for 16 days and the H$_2$ GTR value before and after 4 MPa hydrogen impact for 16 days of all samples, respectively, the insets show the high-pressure autoclave for this test and the pressure gauge; (c and d) CO$_2$ and O$_2$ GTRs of PVA and PVA–20PA samples and instrument-generated O$_2$ and CO$_2$ permeation curves for PVA and PVA–20PA samples, respectively; (e) stress–strain curves of PVA and the PVA–PA samples; (f) tensile strengths and elastic moduli of PVA and the PVA–PA samples; (g) elongation at the break of PVA and the PVA–PA samples; (h) the digital image comparison of the coated and uncoated pipelines by the thin composite film PVA–20PA; and (i) the high-pressure hydrogen resistance mechanism of PVA and the PVA–PA composite film.

microscopic level, with no evidence of microcracks, blistering, or delamination (Fig. S15b). This indicates that the wrinkling is a macroscopic, substrate-level phenomenon that does not compromise the intrinsic structure or continuity of the composite coating itself. The retention of a defect-free surface morphology provides a direct structural explanation for the outstanding preservation of the hydrogen barrier property after the aggressive high-pressure test.

Other performances were explicitly investigated as well. The optimal specimen, PVA–20PA, also presents similarly decreased CO$_2$ and O$_2$ permeability compared to pure PVA, with extremely low GTR values of 0.52 and 0.346 cm^3 m^{-2}·24 h^{-1}·0.1 MPa^{-1}, respectively, suggesting comprehensive and outstanding gas barrier properties (Fig. 4c). The corresponding permeation curves were captured and are plotted in Fig. 4d. The mechanical strength of six samples is revealed and compared in stress–strain curves. Pure PVA possesses a tensile strength of 41.61 MPa and an elongation at break of

305.14% (Fig. 4e–g). The tensile strength value exhibits a moderately increasing tendency, reaching 78.02 MPa for PVA–20PA, while its elongation at break percentage experiences a slight change to 312.4%. The denser H-bond and P–O–C covalent bond crosslinking network formation caused by the complete reaction between PVA and PA contributes to this reasonable trend.[11,51] In comparison, further addition of PA leads to a decreased tensile strength but an increased toughness for the rest of the samples, making more ductile materials. This is because excessive PA incorporation will bring about the exposure of numerous unreacted phosphorous hydroxyl groups to act as plasticizers,[52] as stated in the previous section, leading to a highly mobilized PVA chain and a gradually loosening crosslinking network. Concurrently, an exceedingly high crosslink density can lead to a heterogeneous network architecture and increased brittleness, where stress concentration at microstructural defects facilitates earlier failure. Therefore, the decline in tensile strength at higher PA

loadings is a result of the competing effects between network reinforcement induced by crosslinking and the detrimental plasticization and embrittlement induced by an overabundance of the crosslinker, which is disadvantageous for improving tensile strength.[40]

Additionally, this thin film can be sprayed on the inner wall of the pipeline made of steel 20 (OD = 15 mm, wall thickness = 1 mm, as shown in Fig. 4h), which is mostly applied in hydrogen transportation, based on ICS 77.140.50. It is, therefore, reasonable to deduce that when applied to metallic substrates such as carbon steel, the PVA–PA composite film is expected to maintain comparable barrier performance owing to its strong interfacial adhesion and chemical compatibility with metal oxides. The abundant hydroxyl and phosphate groups in PA can chelate surface Fe^{3+}/Fe^{2+} ions[53] and form a thin phosphate interphase, analogous to a conversion coating, thereby enhancing coating adhesion and preventing under-film corrosion. The hydrogen-bonded and covalently crosslinked PVA–PA network further suppresses interfacial microvoid formation, which is critical for maintaining long-term barrier stability under cyclic pressurization. As demonstrated in Fig. 4h, the film adheres uniformly to the steel inner wall without peeling or cracking. These results suggest that the coating structure and interfacial chemistry can be effectively translated to practical metallic pipeline applications, ensuring durable hydrogen impermeability.

2.4 Simulations

According to the MD simulation method, PVA composite films with three representative PA incorporation levels were constructed. The corresponding film properties, including the FFV, porosity, and pore size distribution based on the simulation results, are presented in Fig. 5a–c. Consistent with the experimental results, the PVA–20PA sample exhibits the lowest FFV of 9.58%, while its porosity follows the same trend, reaching merely 0.37341%. The green curve (PVA) exhibits a broader and less symmetric profile, with its maximum located at around 4 nm, suggesting a wider pore size distribution and the coexistence of mesopores and macropores. In contrast, the orange curve (PV–20PA) shows a unimodal distribution with a sharp peak centred at approximately 2 nm, indicating a relatively uniform pore structure. The FFV and pore size distribution simulation results of other samples are also presented in Fig. S16–S18. In addition, the number of hydrogen bonds exhibits a decreasing trend with increasing PA loading (Fig. 5d) once the film reaches dynamic equilibrium ($t \geq 2$ ns). This is attributed to the consumption of –OH groups by crosslinking and the replacement of PVA–PVA H-bonds. The information on the angle and length of the hydrogen bonds of different PVA–PA composite films is provided in Fig. S18 and S19.

It is noted that the absolute FFV values obtained from MD simulations are consistently higher than those from PALS measurements. This discrepancy is well-documented in the literature and originates from the fundamental differences in

their definitions: MD computes the total geometric void space accessible to a small probe, while PALS selectively quantifies the volume fraction of discrete nanoscale holes that can trap a positronium, which are the very sites governing gas molecule diffusion. Consequently, the PALS-FFV is the key parameter directly correlated with experimental permeability trends, whereas the MD-FFV and its derived pore size distribution provide critical complementary insights into the nanostructural evolution and relative compactness induced by crosslinking.

Then, different permeants (water and hydrogen molecules) were selected to elucidate the atomic-level interactions and diffusion pathways within hydrogen barrier films. The molecular dynamics simulation snapshot in Fig. 5e illustrates the migration of water molecules from the bulk water phase (left) into the PVA-based composite film (right). In the bulk phase, water molecules are densely packed, forming a continuous hydrogen-bonding network. Upon approaching the film interface, they permeate into the polymer matrix through interconnected free-volume regions, diffusing along tortuous pathways formed by PVA chains and crosslinking nodes. The movement of water molecules within the film is severely constrained compared to that in the bulk phase. The mean-squared displacement (MSD) curves illustrated in Fig. 5f show that the water diffusivity follows the order: PVA > PVA–5PA > PVA–50PA ≈ PVA–20PA. The covalent–noncovalent hybrid network reduces the fractional free volume and enhances transient binding, indicating that PA crosslinking markedly suppresses water mobility. The MD simulation snapshots of water molecules' permeation into other samples are presented in Fig. S20.

Fig. 5g displays the MD simulation of H_2 permeation into a PVA–20PA film under a 4 MPa hydrogen atmosphere within 12 ns. Depth-resolved MD snapshots of H_2 in the film are shown in Fig. 5h. In the 0–1 nm interfacial slab, hydrogen molecules accumulate and are transiently trapped, forming a dense near-surface layer. In the 1–2 nm slab, the population drops to sparse isolated molecules with no connected pathways, indicating a steep concentration gradient and an ultra-short penetration length (∼≤1 nm). This depth decay directly reflects a compact PVA crosslinking network constructed by hybrid noncovalent and covalent interactions that suppresses H_2 ingress beyond the immediate interface. By contrast, at identical exposure times and pressures, all comparator PVA films exhibit a deeper hydrogen penetration depth than the optimum sample (beyond the 1–2 nm slab, as shown in Fig. S21–S23), indicating a looser network with a larger fractional free volume and faster ingress of hydrogen.

Besides, the trend of change in the number of hydrogen molecules permeated during the simulation time period is given in Fig. 5i. Pure PVA shows the largest, near-linear increase before a mild plateau; PVA–5PA closely follows. PVA–50PA exhibits a much slower growth. In sharp contrast, the minimal rise for PVA–20PA suggests an optimally compact covalent and noncovalent network that strongly limits diffusion. The hydrogen MSD curves in Fig. S24 also follow the
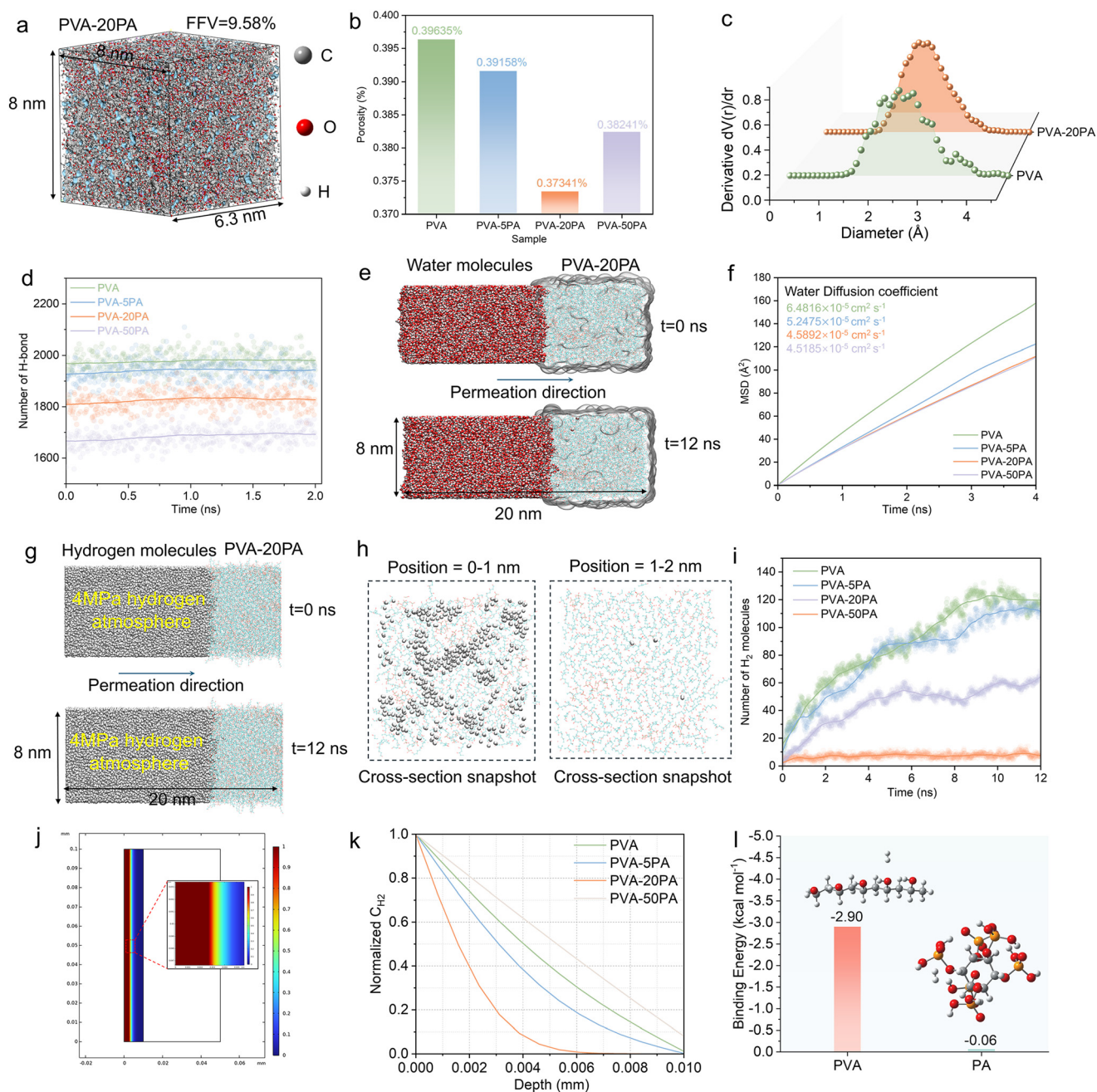
Fig. 5 (a) The FFV molecular simulation model of PVA–20PA; (b and c) the porosity and pore size distribution based on the simulation results of various PVA–PA films, respectively; (d) variation in the hydrogen bonding number of PVA composite systems after dynamical equilibrium; (e) snapshots of the MD simulation of the water permeation process of the PVA–20PA film; (f) MSD curves of PVA chains in the composites as a function of time are employed to analyze the water diffusion coefficient, the insets show the corresponding calculated water diffusion coefficient; (g) snapshots of the MD simulation of the 4 MPa hydrogen permeation process of the PVA–20PA composite film; (h) visualization of hydrogen permeation at different positions within the film; (i) the number of permeated hydrogen molecules in the PVA–20PA composite film; (j and k) 2D plot and line plot of the hydrogen concentration (in mol m^{-3}) in PVA–20PA at t = 60 d, respectively; and (l) the DFT calculations for the binding energies of H$_2$ to PVA and PA, the insets present the molecular structures of the PVA and PA.

trend: PVA > PVA–5PA > PVA–50PA > PVA–20PA, which quantitatively substantiates the differences in H$_2$ permeation among the four films from a simulation perspective.

Subsequently, to establish a predictive computational fluid dynamics (CFD) model for macroscopic transport behaviour, we defined its core inputs using key microstructural parameters derived from MD simulations, spanning the following

critical statuses: (1) the diffusion coefficient within the material and (2) the porosity characterizing the internal structure. These parameters, originating from MD simulations, were directly applied to initialize the corresponding physical fields and define the porous media properties in the CFD simulation. The simulation was performed on the symmetrical half of the pipe's inner wall cross-section, as illustrated in Fig.

S25 (assuming a coating thickness of 0.01 mm), using a time-dependent solver with a time range of 60 days. Fig. 5g and h displays the 2D distribution of the hydrogen concentration (C_{H_2}) in PVA–20PA-coated API X52 steel (base metal) at the end of the simulation (t = 60 d) and a line plot of the hydrogen concentration across various composite coatings along the permeation direction, respectively. Obviously, the colour gradient along the 0–0.01 mm depth axis (right legend) quantifies the permeation intensity, with saturated hues indicating the peak concentration at a 0 mm depth and fading tones toward the film-substrate interface (0.01 mm), confirming the strong shielding ability of the PVA–20PA composite coating against hydrogen molecules (Fig. 5h). PVA–20PA shows the sharpest normalized C_{H_2} decrease among PA-incorporated samples, which is also in agreement with the experimental results (Fig. 3a). The 2D plot of the hydrogen concentration (in mol m^{-3}) in other specimens is given in Fig. S26–S28.

The binding energies of PVA–H$_2$ and PA–H$_2$, investigated by DFT calculations, are illustrated in Fig. 5l, both of which (−2.90 kcal mol^{-1} and −0.06 kcal mol^{-1}, respectively) prove their weak interactions with hydrogen molecules. This result verifies that PVA or PA itself possesses no significant affinity for hydrogen molecules. Contrastingly, the high binding energy between PVA and PA (−40.92 kcal mol^{-1}) is the key mechanism for enhanced H$_2$ barrier properties, attributed to the formation of a tightly crosslinked, low-free-volume composite network. Therefore, PA functions primarily as a crosslinking agent for PVA. Its effectiveness stems from forming a robust, cohesive network with PVA, rather than directly interacting with or blocking H$_2$ molecules.

3 Conclusion

In this work, we have successfully designed and fabricated a highly effective poly(vinyl alcohol) (PVA)-based composite thin film using a facile spraying method, incorporating phytic acid (PA) as a bio-derived crosslinker to enhance the crosslinking density. Consequently, the optimized PVA–20PA composite film achieves an unprecedentedly low hydrogen gas transmission rate (H$_2$ GTR) of 0.518 cm^3 m^{-2}·24 h^{-1}·0.1 MPa^{-1}, representing a ∼75.5% reduction compared to pure PVA. The synergistic interplay of abundant intermolecular (hydrogen bonding and phosphonate bonds) interactions within the PVA–PA system induces the formation of a densely crosslinked network. This network significantly restricts polymer chain mobility, contributing to a remarkable reduction in the FFV to merely 0.6509%, as comprehensively elucidated through combined experimental characterizations (FTIR, XPS, PALS, and XRD) and theoretical simulations (DFT and MD). Crucially, the film demonstrates outstanding high-pressure stability, maintaining a low H$_2$ GTR of 0.966 cm^3 m^{-2}·24 h^{-1}·0.1 MPa^{-1} even after prolonged exposure to a demanding 4 MPa hydrogen environment for 16 days. Furthermore, the composite film exhibits robust mechanical properties, with a high tensile strength of 78.02 MPa, and possesses superior barrier capabilities against other gases (CO$_2$ and O$_2$). This work not only advances the development of high-performance

hydrogen barrier materials but also provides valuable insights into the design of functional composites for industrial applications.

4 Experimental section

4.1 Materials

Polyvinyl alcohol, PVA-1799 (degree of polymerization: 1700, degree of hydrolysis: 99%, analytical purity), was purchased from Shanghai Bide Pharmaceutical Technology Co., Ltd., China. Phytic acid (PA, 50 wt% aqueous solution) was obtained from Xiensi Opd Technology Co., Ltd. Graphite papers were bought from Hebei Jingtan Technology Co., Ltd. The steel pipe was provided by Tianjin Hongda Metal Materials Sales Co., Ltd.

4.2 Preparation of PVA–PA composite thin films

Initially, a 1 wt% PVA aqueous solution was prepared by dissolving the PVA powder in water *via* 90 °C water-bath heating for 1.5 hours. Then, a certain amount of a PA aqueous solution was added to the PVA solution with continuous stirring for another 15 min, followed by ultrasonic treatment to ensure a complete and homogeneous mixture. The as-prepared solution was sprayed on graphite paper by employing a facile spray-coating process using a spraying gun with an air-assisted atomizing nozzle at a spraying pressure of 4 bar. The nozzle-to-substrate distance was approximately 15 cm, and the substrate (graphite paper) temperature was maintained at 140 °C on a heating platform to accelerate solvent evaporation and crosslinking. The spray gun was reciprocally moved across the substrate from the left to the right until the entire surface was uniformly coated, and the process was repeated while allowing the solvent to fully evaporate between passes, which was defined as one spray cycle. Typically, 15–20 cycles were required to obtain a coating with a thickness of about 5–10 μm for further characterization. The composite thin films with 5–50 wt% PA (the proportion of the actual amount of PA in PVA) were denoted as PVA–5PA to PVA–50PA, respectively.

4.3 Characterization

Film morphologies and structural features were investigated employing a scanning electron microscope (SEM, Apreo S LoVac). Energy-dispersive X-ray (EDX) spectra linked to SEM were also obtained to analyse the elemental weights and atomic percentages. The valence of elements and bonding details of PVA and PVA–PA composite films were investigated by X-ray photoelectron spectroscopy (XPS, Thermo Fisher Scientific ESCALAB Xi+). The chemical groups of films were examined by a Fourier transform infrared (FT-IR) spectrometer (PerkinElmer, iS50) in the range of 450–4000 cm^{-1}. An X-ray diffractometer (XRD, Smartlab, maximum output power: ≥3 kW, voltage: ≥60 kV, current: ≥60 mA) was employed to detect the crystal structures of the composite film with the Bragg angle ranging from 5° to 40°. Thermogravimetric analysis (TGA, TG 209 F3 Tarsus) was employed to evaluate the

thermal stability of the composite film under a N_2 atmosphere between 25 and 600 °C with a heating rate of 10–20 °C. The differential scanning calorimetry (DSC) technique was conducted to determine the thermal properties of the prepared coatings. It was conducted using a Netzsch Instruments DSC 200F3 in a nitrogen atmosphere to prevent sample oxidation. Firstly, the sample was heated from 40 °C to 200 °C at a rate of 10 °C min^{-1}, held at 200 °C for 5 min and then cooled to 40 °C. Secondly, the sample was again heated to 200 °C at 10 °C min^{-1}. The water contact angle was measured by a contact angle measuring system (Attention Theta Lite) based on the sessile drop measuring method, and the average WCA value was obtained by testing five different positions on each surface with a water volume of 10 μL at room temperature (25 °C). The H_2 GTR values of various composite coatings were tested by the GPT-H201 (Jinan Saicheng) gas permeability machine at 106 kPa (pressure) and 25 °C. The tests were conducted in accordance with the Chinese National Standard GB/T 19789-2021. The sample preparation and subsequent testing followed three main steps. Firstly, some vacuum grease was smeared around the cavity and covered by filter paper. Then, the prepared sample was placed on the test bench and ensured that the size of the covered area was larger than that of the cavity. Finally, the inner and outer chambers of the container and the entire system were evacuated until the targeted vacuum degree (around 26 Pa) was reached; the vacuuming process lasted for at least 3 h to eliminate any gas and water vapour adsorbed by the sample, and test gas was introduced into the outer chamber of the container. After this process, permeation happened under the action of the differential pressure gradient, and the GTR value was calculated by a plot generated by the software linked to the machine by monitoring the pressure on the lower-pressure side. The positron annihilation lifetime spectrometry (PALS) test employed two self-developed BaF scintillator detectors and the standard NIM plugin from EG&G, USA, to measure the positron annihilation lifetime spectra by the fast-slow conformal measurement technique. A Kapton membrane with a 7.5 μm thickness with sealed ^{22}Na was used as the positron source with an activity of about 10 μCi. A "sample-source-sample" sandwich structure was adopted for the test, with the source and sample placed in the middle of the two detectors. The time resolution of the spectrometer was 210 ps, 2 million total counts were collected for each lifetime spectrum, and the general Lifetime 9.0 software was used for data processing.

Author contributions

Sicheng Yuan: conceptualization, methodology, software, validation, formal analysis, data curation, visualization, writing – original draft, writing – review & editing, data curation, investigation. Jintao Wei: conceptualization, data curation, investigation. Junhao Zhou: formal analysis, investigation. Sheng Zhang: conceptualization, data curation. Baiwen Wang: data curation, formal analysis. Yanji Zhu: funding acquisition. Huaiyuan Wang: validation, funding acquisition, supervision.

Conflicts of interest

The authors declare no conflict of interest.

Data availability

The data supporting this article have been included as part of the supplementary information (SI). The authors will supply other relevant data upon reasonable request.

Supplementary information is available. See DOI: https://doi.org/10.1039/d5im00279f.

Acknowledgements

References

1 N.-E. Laadel, M. El Mansori, N. Kang, S. Marlin and Y. Boussant-Roux, Permeation barriers for hydrogen embrittlement prevention in metals – A review on mechanisms, materials suitability and efficiency, *Int. J. Hydrogen Energy*, 2022, **47**, 32707–32731.

2 S. Singh, S. Jain, V. Ps, A. K. Tiwari, M. R. Nouni, J. K. Pandey and S. Goel, Hydrogen: A sustainable fuel for future of the transport sector, *Renewable Sustainable Energy Rev.*, 2015, **51**, 623–633.

3 C. Zhang, Y. Shao, W. Shen, H. Li, Z. Nan, M. Dong, J. Bian and X. Cao, Key technologies of pure hydrogen and hydrogen-mixed natural gas pipeline transportation, *ACS Omega*, 2023, **8**, 19212–19222.

4 H. Li, X. Cao, Y. Liu, Y. Shao, Z. Nan, L. Teng, W. Peng and J. Bian, Safety of hydrogen storage and transportation: An overview on mechanisms, techniques, and challenges, *Energy Rep.*, 2022, **8**, 6258–6269.

5 X. Li, P. Bandyopadhyay, M. Guo, N. H. Kim and J. H. Lee, Enhanced gas barrier and anticorrosion performance of boric acid induced cross-linked poly(vinyl alcohol-co-ethylene)/graphene oxide film, *Carbon*, 2018, **133**, 150–161.

6   P. Bandyopadhyay, W. B. Park, R. K. Layek, M. E. Uddin, N. H. Kim, H.-G. Kim and J. H. Lee, Hexylamine functionalized reduced graphene oxide/polyurethane nanocomposite-coated nylon for enhanced hydrogen gas barrier film, *J. Membr. Sci.*, 2016, **500**, 106–114.

7   Y. Sun, H. Lv, W. Zhou and C. Zhang, Research on hydrogen permeability of polyamide 6 as the liner material for type IV hydrogen storage tank, *Int. J. Hydrogen Energy*, 2020, **45**, 24980–24990.

8   S. Saha, W. Son, N. H. Kim and J. H. Lee, Fabrication of impermeable dense architecture containing covalently stitched graphene oxide/boron nitride hybrid nanofiller reinforced semi-interpenetrating network for hydrogen gas barrier applications, *J. Mater. Chem. A*, 2022, **10**, 4376–4391.

9   C. Liu, H. Li, J. Zhu, X. Huan, K. Xu, H. Geng, X. Guo, L. Ge, X. Jia, X. Yang and H. Wang, Non-covalent and covalent-synergistical-interaction assembled GO self-supporting membrane with excellent alignment for ultrahigh H_2 barrier applications, *Composites, Part B*, 2024, **283**, 111652.

10 J. Li, Y. Li, Y. Song, S. Niu and N. Li, Ultrasonic-assisted synthesis of polyvinyl alcohol/phytic acid polymer film and its thermal stability, mechanical properties and surface resistivity, *Ultrason. Sonochem.*, 2017, **39**, 853–862.

11 R. Kumar, K. Park, K. Ahn, J. R. Ansari, K. Sadeghi and J. Seo, Maleic acid crosslinked starch/polyvinyl alcohol blend films with improved barrier properties for packaging applications, *Int. J. Biol. Macromol.*, 2024, **271**, 132495.

12 Y. Lei, L. Liu, C. A. Scholes and S. E. Kentish, Crosslinked PVA based polymer coatings with shear-thinning behaviour and ultralow hydrogen permeability to prevent hydrogen embrittlement, *Int. J. Hydrogen Energy*, 2024, **54**, 947–954.

13 D. Rahmadiawan, S.-C. Shi and W.-T. Zhuang, Reinforcing polyvinyl alcohol films with layered double hydroxide and tannic acid to enhance tensile strength, tribological performance, and corrosion resistance in biomedical coating applications, *Mater. Res. Express*, 2024, **11**, 115302.

14 K. Park, Y. Oh, P. K. Panda and J. Seo, Effects of an acidic catalyst on the barrier and water resistance properties of crosslinked poly (vinyl alcohol) and boric acid films, *Prog. Org. Coat.*, 2022, **173**, 107186.

15 J. H. Woo, N. H. Kim, S. I. Kim, O.-K. Park and J. H. Lee, Effects of the addition of boric acid on the physical properties of MXene/polyvinyl alcohol (PVA) nanocomposite, *Composites, Part B*, 2020, **199**, 108205.

16 L. Wen, Y. Liang, Z. Lin, D. Xie, Z. Zheng, C. Xu and B. Lin, Design of multifunctional food packaging films based on carboxymethyl chitosan/polyvinyl alcohol crosslinked network by using citric acid as crosslinker, *Polymer*, 2021, **230**, 124048.

17 J. Wang, Z. Li, J. Liu, H. Wu, M. Guo, W. Wang, C. Yan and Q. Li, Synergistic enhancement of barrier performance in silanized modified hemicellulose/PVA composite films through oxalic acid crosslinking, *Ind. Crops Prod.*, 2024, **215**, 118644.

18 K. Liu, S. Huang, F. Duan and J. Wang, Preparation and characterization of high barrier coating of citric acid crosslinked polyvinyl alcohol and nano-SiO2, *J. Coat. Technol. Res.*, 2024, **21**, 1729–1743.

19 L. Li, X. Xu, B. Wang, P. Song, Q. Cao, Y. Yang, Z. Xu and H. Wang, Structure, chain dynamics and mechanical properties of poly(vinyl alcohol)/phytic acid composites, *Compos. Commun.*, 2021, **28**, 100970.

20 J. Li, C. Wang, T. Miao, S. Guo, Y. Tong and L. Zhang, Airflow-assisted acoustic spray coating for suppressing pinhole defects on photoresist film, *Mater. Sci. Semicond. Process.*, 2025, **196**, 109657.

21 K. Huang, Y. Wang, Z. Xu, Z. Zou, Q. Tang, H. Li and D. Peng, Novel intelligent packaging films based on starch/PVA with Cu-ICA nanocrystal as functional compatibilizer for monitoring food freshness, *Int. J. Biol. Macromol.*, 2024, **271**, 132373.

22 X. Hong, Y. Zheng, Y. Shi, W. Zheng, F. Lin and L. Xiong, A facile strategy for constructing lightweight, fire safety and compression resistance poly(vinylalcohol) aerogels with highly-efficient expansible graphene oxide/layered double hydroxides hybrid synergistic flame retardant, *J. Colloid Interface Sci.*, 2023, **650**, 686–700.

23 A. A. Menazea, M. H. El-Newehy, B. M. Thamer and M. E. El-Naggar, Preparation of antibacterial film-based biopolymer embedded with vanadium oxide nanoparticles using one-pot laser ablation, *J. Mol. Struct.*, 2021, **1225**, 129163.

24 Y. Ning, R. Liu, W. Chi, X. An, Q. Zhu, S. Xu and L. Wang, A chitosan derivative/phytic acid polyelectrolyte complex endowing polyvinyl alcohol film with high barrier, flame-retardant, and antibacterial effects, *Int. J. Biol. Macromol.*, 2024, **259**, 129240.

25 K. S. Hemalatha, K. Rukmani, N. Suriyamurthy and B. M. Nagabhushana, Synthesis, characterization and optical properties of hybrid PVA–ZnO nanocomposite: A composition dependent study, *Mater. Res. Bull.*, 2014, **51**, 438–446.

26 L. Zeng, B. Liu and G. Gao, Physically crosslinked polyvinyl alcohol/chitosan-phytic acid hydrogels for wearable sensors with highly conductive, recyclable and antibacterial properties, *Sci. China Mater.*, 2023, **66**, 4062–4070.

27 M. H. Rahmani, A. Dehghani, G. Bahlakeh and B. Ramezanzadeh, Introducing GO-based 2D-platform modified via phytic acid molecules decorated by zeolite imidazole ZIF-9 MOFs for designing multi-functional polymeric anticorrosive system; DFT-D computations and experimental studies, *J. Mol. Liq.*, 2022, **364**, 119945.

28 K. Jiang and X. Wang, Preparation and application of maleic acid crosslinked polyvinyl alcohol/mica coating for barrier paper, *Prog. Org. Coat.*, 2022, **170**, 106937.

29 D. K. Patel, K. Ganguly, S. D. Dutta, T. V. Patil, A. Randhawa and K. T. Lim, Highly stretchable, adhesive, and biocompatible hydrogel platforms of tannic acid functionalized spherical nanocellulose for strain sensors, *Int. J. Biol. Macromol.*, 2023, **229**, 105–122.

30 Y. Li, Y. Song, J. Li, Y. Li, N. Li and S. Niu, A scalable ultrasonic-assisted and foaming combination method preparation polyvinyl alcohol/phytic acid polymer sponge with thermal stability and conductive capability, *Ultrason. Sonochem.*, 2018, **42**, 18–25.

31 N. Mehra, L. Mu and J. Zhu, Developing heat conduction pathways through short polymer chains in a hydrogen bonded polymer system, *Compos. Sci. Technol.*, 2017, **148**, 97–105.

32 X.-F. Qian, J. Yin, J.-C. Huang, Y.-F. Yang, X.-X. Guo and Z.-K. Zhu, The preparation and characterization of PVA/Ag$_2$S nanocomposite, *Mater. Chem. Phys.*, 2001, **68**, 95–97.

33 Y. Fang, S. Xiong, H. Huang, J. Zhu, J. Yu, Y. Wang and Z. Hu, Polydopamine nanotube for dual bio-inspired strong, tough, and flame retarding composites, *Composites, Part B*, 2020, **197**, 108184.

34 Z. Zhang, X. Li, Z. Ma, H. Ning, D. Zhang and Y. Wang, A facile and green strategy to simultaneously enhance the flame retardant and mechanical properties of poly(vinyl alcohol) by introduction of a bio-based polyelectrolyte complex formed by chitosan and phytic acid, *Dalton Trans.*, 2020, **49**, 11226–11237.

35 Z. Zhang, Z. Zhou, J. Huang and Y. Wang, A flame retardant poly vinyl alcohol/graphene oxide/phytic acid composite for a quick response and ultra-long fire alarm, *J. Mater. Chem. A*, 2024, **12**, 6050–6066.

36 B. He, S. Wu, Q. Zhao, Y. Meng, X. Tang, S. Yu, L. Yang, Y. Xu, T. Gao and D. Xiao, Utilizing the cross-linked effect and reconstruction strategy of phytic acid to build Fe-Co-Ni trimetallic amorphous carbon-matrix compounds as efficient oxygen evolution catalyst, *J. Colloid Interface Sci.*, 2023, **629**, 1003–1014.

37 X. Fan, R. Zhang, S. Sui, X. Liu, J. Liu, C. Shi, N. Zhao, C. Zhong and W. Hu, Starch-based superabsorbent hydrogel with high electrolyte retention capability and synergistic interface engineering for long-lifespan flexible zinc–air batteries, *Angew. Chem., Int. Ed.*, 2023, **62**, e202302640.

38 D. Damodar, U. Mahanta and A. S. Deshpande, N-doped MWCNTs from catalyst-free, direct pyrolysis of commercial glue, *Mater. Chem. Phys.*, 2021, **262**, 124319.

39 X. Zhou, H. Huang, R. Zhu, R. Chen, X. Sheng, D. Xie and Y. Mei, Green modification of graphene oxide with phytic acid and its application in anticorrosive water-borne epoxy coatings, *Prog. Org. Coat.*, 2020, **143**, 105601.

40 C. Liu, R. Zhang, Y. Wang, C. Wei, F. Li, N. Qing and L. Tang, Highly adhesive chitosan/poly(vinyl alcohol) hydrogels via the synergy of phytic acid and boric acid and their application as highly sensitive and widely linear strain sensors, *Mater. Horiz.*, 2023, **10**, 3488–3498.

41 R. Hu, J. Zhao, Y. Wang, Z. Li and J. Zheng, A highly stretchable, self-healing, recyclable and interfacial adhesion gel: Preparation, characterization and applications, *Chem. Eng. J.*, 2019, **360**, 334–341.

42 F. Cao, J. Wei, J. Dong and W. Ke, The corrosion inhibition effect of phytic acid on 20SiMn steel in simulated carbonated concrete pore solution, *Corros. Sci.*, 2015, **100**, 365–376.

43 C.-F. Zhu, J.-X. Zhang, S.-P. Qian and T.-H. Pan, Sustainable flame-retardant and tough poly (vinyl alcohol) films with phytic acid and biochar: a simple and effective approach, *Chin. J. Polym. Sci.*, 2025, **43**, 1333–1345.

44 V. A. Kong, T. A. Staunton and J. E. Laaser, Effect of cross-link homogeneity on the high-strain behavior of elastic polymer networks, *Macromolecules*, 2024, **57**, 4670–4679.

45 G. Choudalakis and A. D. Gotsis, Free volume and mass transport in polymer nanocomposites, *Curr. Opin. Colloid Interface Sci.*, 2012, **17**, 132–140.

46 J. Wu, S. Japip and T.-S. Chung, Infiltrating molecular gatekeepers with coexisting molecular solubility and 3D-intrinsic porosity into a microporous polymer scaffold for gas separation, *J. Mater. Chem. A*, 2020, **8**, 6196–6209.

47 R. Rudra, V. Kumar and P. P. Kundu, Acid catalysed cross-linking of poly vinyl alcohol (PVA) by glutaraldehyde: Effect of crosslink density on the characteristics of PVA membranes used in single chambered microbial fuel cells, *RSC Adv.*, 2015, **5**, 83436–83447.

48 G. I. Andrade, E. F. Barbosa-Stancioli, A. A. P. Mansur, W. L. Vasconcelos and H. S. Mansur, Small-angle X-ray scattering and FTIR characterization of nanostructured poly (vinyl alcohol)/silicate hybrids for immunoassay applications, *J. Mater. Sci.*, 2007, **43**, 450–463.

49 J. R. Fekete, J. W. Sowards and R. L. Amaro, Economic impact of applying high strength steels in hydrogen gas pipelines, *Int. J. Hydrogen Energy*, 2015, **40**, 10547–10558.

50 H. Wang, Z. Tong, G. Zhou, C. Zhang, H. Zhou, Y. Wang and W. Zheng, Research and demonstration on hydrogen compatibility of pipelines: A review of current status and challenges, *Int. J. Hydrogen Energy*, 2022, **47**, 28585–28604.

51 Z. Liu, Z. Qin, H. Jia, J. Xu, M. Liu and Z. Hou, Dual-crosslinked starch–poly(ester urethane)–oligochitosan films with high starch content: Application as biodegradable food packaging, *Food Packag. Shelf Life*, 2023, **37**, 101064.

52 Z. Wan, R. Qu, Y. Sun, Y. Gao, G. Gao, K. Chen and T. Liu, Physically crosslinked polyvinyl alcohol, phytic acid and glycerol hydrogels for wearable sensors with biocompatibility, antimicrobial stability and anti-freezing, *Eur. Polym. J.*, 2024, **211**, 112974.

53 A. P. M. Bloot, D. L. Kalschne, J. A. S. Amaral, I. J. Baraldi and C. Canan, A review of phytic acid sources, obtention, and applications, *Food Rev. Int.*, 2023, **39**, 73–92.